1

Introduction to Hybrid Organic–Inorganic Perovskites

1.1 Perovskite Oxides

Perovskite is a calcium titanium oxide mineral, which has the chemical formula of $CaTiO_3$. It was discovered in 1839 by the Prussian mineralogist Gustav Rose in a piece of skarn collected from the Ural Mountains and named in honour of the Russian Count, Lev A. Perovskiy [1]. Nowadays, perovskites broadly denote any materials that have the same type of structure as $CaTiO_3$, and their general chemical formula can be expressed as ABX_3 [2]. The A and B represent two metal ions that have different ionic radii, and the X denotes an anion that is six-coordinated to the B-site. Adjacent BX_6 octahedra are three dimensionally linked via sharing their corners to generate a framework structure in which the A-site counterbalancing cations are located in the framework cavities (Figure 1.1). The perovskite structure can also be considered as a cubic close-packed system in which the A- and X-sites are stacked in a cubic-close-packed manner along the body-diagonal direction.

Perovskite oxides have diverse compositions, which can accommodate a great deal of elements in the periodic table, and the corresponding chemical variations enable many physical properties that have important industrial applications [3]. Perovskite materials were only limited to applications as pigments initially; however, the surge of military need for ferroelectric materials during the 1940s led to the invention of $BaTiO_3$ and the start of the electronic era of perovskites [4]. The crystal structure of $BaTiO_3$ was solved by Helen D. Megaw in 1945, and this seminal work initiated the fundamental understanding of structural evolution and associated properties of synthetic perovskite oxides [5]. As illustrated in Figure 1.2a, the B-site Ti^{4+} displaces from the centre of TiO_6 in the ambient trigonal phase of $BaTiO_3$ ($R3m$), which induces the occurrence of spontaneous polarization and therefore ferroelectric ordering. $BaTiO_3$ is one of the most commonly used ferroelectric ceramics in a variety of industrial fields nowadays. Research in 1950s led to the invention of another important perovskite ceramic, lead zirconate titanate ($PbZr_xTi_{1-x}O_3$, PZT, $0 < x < 1$), which is a solid solution of $PbZrO_3$ and $PbTiO_3$ (Figure 1.2b) [6]. PZT shows a striking piezoelectric effect in addition to its intrinsic ferroelectricity and has been being widely utilized as transducers, capacitors, and actuators in industry. Lanthanum manganite ($LaMnO_3$, Figure 1.2c) is another very important perovskite oxide, which

Hybrid Organic-Inorganic Perovskites, First Edition.
Wei Li, Alessandro Stroppa, Zhe-Ming Wang, and Song Gao.

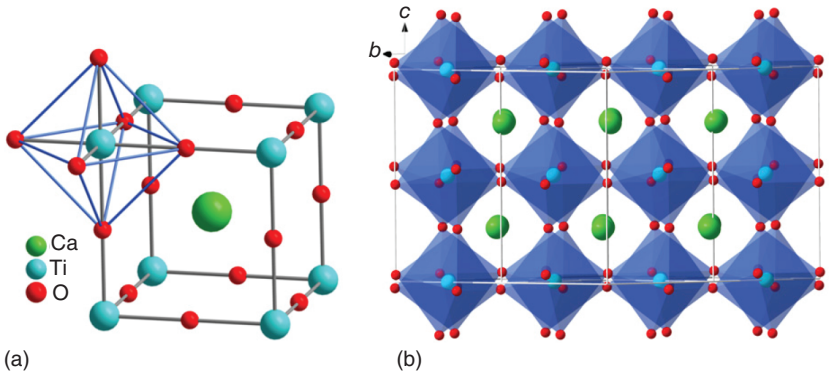

Figure 1.1 Structure of perovskite mineral, $CaTiO_3$. (a) The pseudo-cubic unit and (b) the 3D framework structure. Source: Sasaki et al. 1987 [30]. Reproduced with permission of International Union of Crystallography.

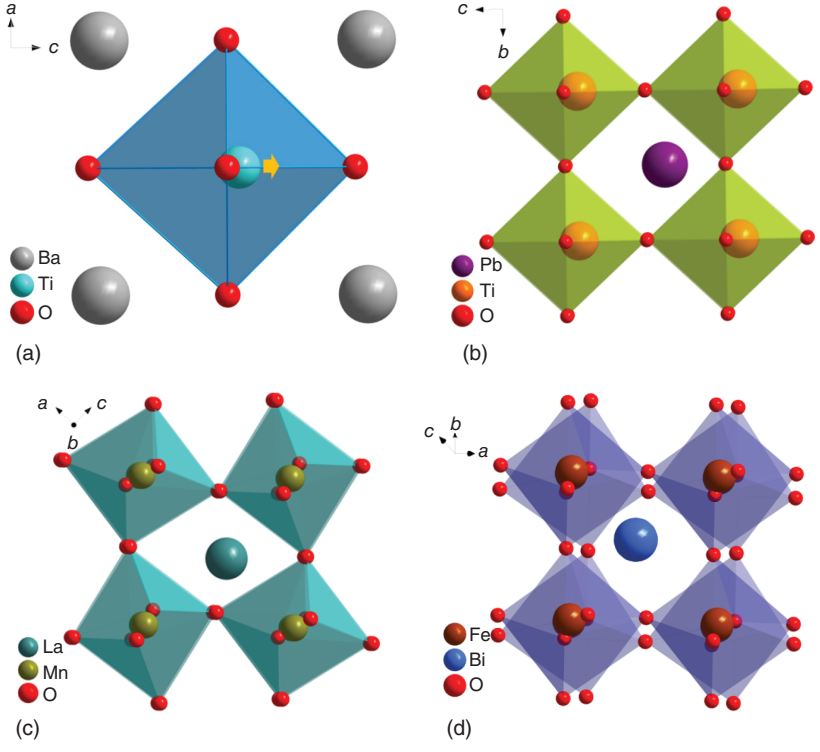

Figure 1.2 Structures of some prototypic perovskite oxides at ambient conditions. (a) $BaTiO_3$, tetragonal, and *P*4*mm*. Source: Megaw 2001 [5]. Reproduced with permission of Springer Nature; (b) $PbTiO_3$, tetragonal, and *P*4*mm*. Source: Glazer and Mabud 1974 [6]. Reproduced with permission of International Union of Crystallography; and (c) $LaMnO_3$, orthorhombic, and *Pnma*. Source: Norby et al. 1995 [7]. Reproduced with permission of Elsevier; (d) $BiFeO_3$, trigonal, *R*3*c*. Source: Frank and Hans 1990 [8]. Reproduced with permission of International Union of Crystallography.

exhibits multiple degrees of freedom induced by the substitution of La^{3+} by Sr^{2+} or Ca^{2+} on the A-site [7]. Such a doping introduces Mn^{3+} in addition to the original Mn^{4+} on the B-site, and these discrete magnetic ground states enable the colossal magnetoresistance effect, which has promising applications in memory devices. In addition to the singular electric or magnetic properties, bismuth ferrite ($BiFeO_3$) can exhibit both ferroelectric and magnetic ordering at ambient conditions to give rise to multiferroicity promising for applications in spintronics [8]. Overall, the enormous chemical availability of perovskite oxides gives rise to their diverse magnetic and electronic properties and corresponding applications.

In terms of synthesis [3], polycrystalline perovskite oxides are normally prepared by high-temperature solid-state reactions by mixing oxide reactants. In this process, some toxic starting oxides, especially PbO, could vaporize during the long reaction time and the generated volatile substances would cause serious safety and environmental problems. To overcome this issue, sol–gel, hydrothermal, and microwave synthesis methods are used to prepare various perovskite oxides. For synthesizing perovskite thin films, which can be integrated into silicon circuits, costly physical vapour deposition and pulsed laser deposition methods are often required.

1.2 Evolution from Perovskite Oxides to Hybrid Organic–Inorganic Perovskites

The A-, B-, and X-sites of the perovskite architecture are not limited to metal cations and oxygen anions, and they can accommodate versatile compositions if the charge balance and lattice match can be maintained. Replacing the A- and/or X-site metal ions with organic amine cations and/or molecular bitopic linkers leads to a sub-class of perovskite materials, namely hybrid organic–inorganic perovskites (HOIPs, Figure 1.3) [9]. Specifically, by introducing the organic molecular cations on the A-site and bitopic inorganic single or molecular anion on the X-sites, several families of hybrid perovskites can be formed, which include halides, azides, cyanides, hypophosphites, and borohydrides [9]. For example, the assembly of methylammonium iodide (CH_3NH_3I) and lead iodide (PbI_2) in hydroiodic acid gives rise to the formation of $MAPbI_3$ (MA = methylammonium) with striking photovoltaic properties (Figure 1.3b) [10]. Additional introduction of bitopic organic molecular linkers on the X-site leads to several families of metal–organic perovskites, which include metal–formate and metal–dicyanamide perovskites with formate and dicyanamide group on the X-site, respectively. For example, mixing methylamine, manganese salt, and formic acid gives rise to magnetic $[MA][Mn(HCOO)_3]$, which has organic components on both the A- and X-sites [11].

Importantly, the incorporation of organic components in the HOIP structures gives them significantly different electronic nature and structural flexibility compared with their oxide counterparts. These unique features could enable striking properties and associated functionalities that are not available in perovskite oxides. In addition, the enormous structural diversity and chemical variability

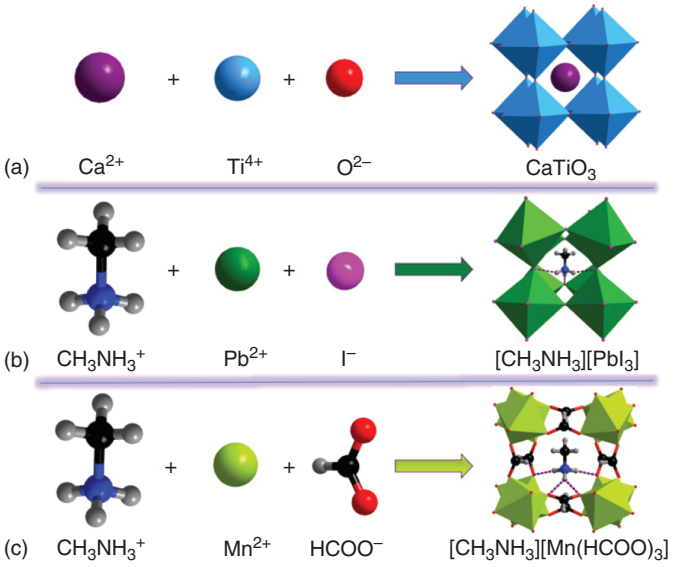

Figure 1.3 Evolution from perovskite oxides to hybrid organic–inorganic perovskites. (a) Perovskite oxide, $CaTiO_3$ [30]; (b) hybrid perovskite with the organic A-site, $[MA][PbI_3]$ [10]; and (c) hybrid perovskite with the organic A- and X-site, $[MA][Mn(HCOO)_3]$ [11]. Colour schemes: C, black; N, blue, O, red; and H, grey. Source: Li et al. 2017 [9]. Reproduced with permission of the Nature Publishing Group.

of HOIPs would be expected to enable versatile physical properties and open up huge opportunities for tuning functionalities via facile bottom-up synthesis.

1.3 Classification and Chemical Variations of HOIPs

In terms of structure, hybrid perovskites can be categorized as several sub-classes, which include ABX_3 perovskites, $A_2BB'X_6$ double perovskites, A_3BX anti-perovskites, ABX_3 hexagonal perovskites, and ABX_3 post-perovskites. The B-site metal ions in many HOIPs are divalent, replacing them with mixed monovalent and trivalent metal ions leading to diverse compounds with the $A_2BB'X_6$ double-perovskite structure, which include halides, azides, cyanides, and formates. Figure 1.4a shows a typical example of hybrid double perovskites, $[TMA]_2[KSc(HCOO)_6]$ (TMA = tetramethylammonium), in which both the K^+ and Sc^{3+} ions are on the B-site [12]. Hybrid anti-perovskites have also been reported, although they are relatively rare. Known examples include a few halides [13, 14] and a family of ternary tetrathiafulvalenium salts (Figure 1.4b) [15]. In addition, there are many ABX_3-type hexagonal perovskites, in which the BX_6 octahedra exhibit a face-sharing mode to form a one-dimensional structure [16]. These hybrid hexagonal perovskites are mainly halides, and Figure 1.4c shows a typical example, $[DABCOH_2][KCl_3]$ [16]. Furthermore, recent studies demonstrate two very rare examples of hybrid ABX_3-type post-perovskites, $(C_5H_{13}NCl)[M(dca)_3]$ ($C_5H_{13}NCl$ = chlorocholine, M^{2+} = Mn^{2+} and Cd^{2+}, and

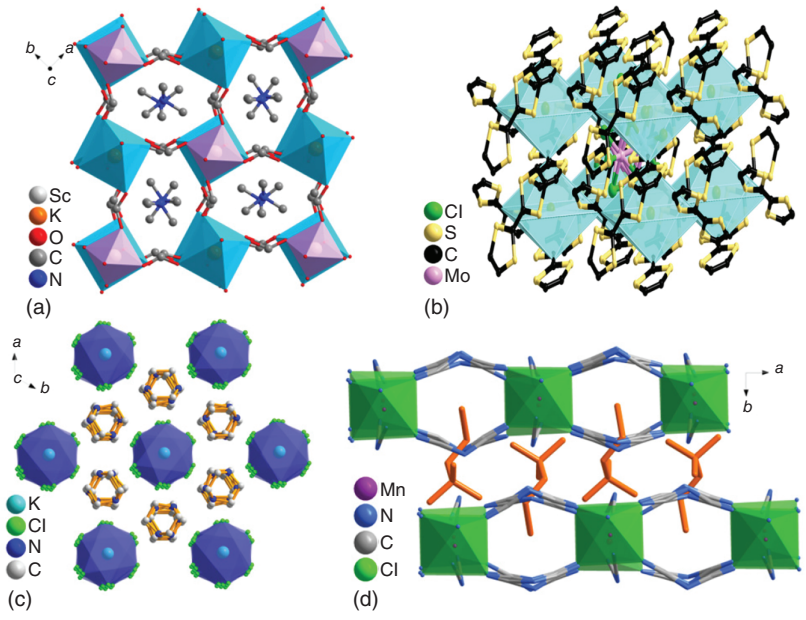

Figure 1.4 Prototypical examples of hybrid organic–inorganic perovskites with double perovskite, anti-perovskite, hexagonal perovskite, and post-perovskite structures. (a) Double perovskite, $[TMA]_2[KSc(HCOO)_6]$. Source: Javier et al. 2015 [12]. Reproduced with permission of American Chemical Society; (b) anti-perovskite, $(TTF^{\bullet})_3[(X)(Mo_6X_{14})]$ ($TTF^{\bullet+}$ = tetrathiafulvalenium; X = C1, Br, and I). Source: Batail 1991 [15]. Reproduced with permission of John Wiley & Sons; (c) hexagonal perovskite, $[DABCOH_2][KCl_3]$. Source: Paton and Harrison 2010 [16]. Reproduced with permission of John Wiley & Sons; (d) post-perovskite, $(C_5H_{13}NCl)[Mn(dca)_3]$. Source: Wang et al. 2019 [17]. Reproduced with permission of American Chemical Society.

dca = dicyanamide), in which adjacent $M(dca)_6$ octahedra are connected to generate anionic layers by sharing their edges and corners two dimensionally and the charge balancing A-site organic cations are intercalated between adjacent layers [17].

1.4 Structure, Symmetry, and Property Features of HOIPs

1.4.1 General Trend

The enormous diversity in organic cations on the A-site, metal ions on the B-site, and bitopic linkers on the X-site offers various combinations of HOIPs, which lead to more than a hundred hybrid perovskites covering a large part of the periodic table. The possible A-site organic groups are summarized in Figure 1.5, which demonstrate that most of them are organic amine cations with monovalent charge [9]. However, there are some organic diamine cations that can also be suitable as the A-site. In addition, few other types of organic cations can also serve as the A-site; for example, triphenylsulfonium is able to template

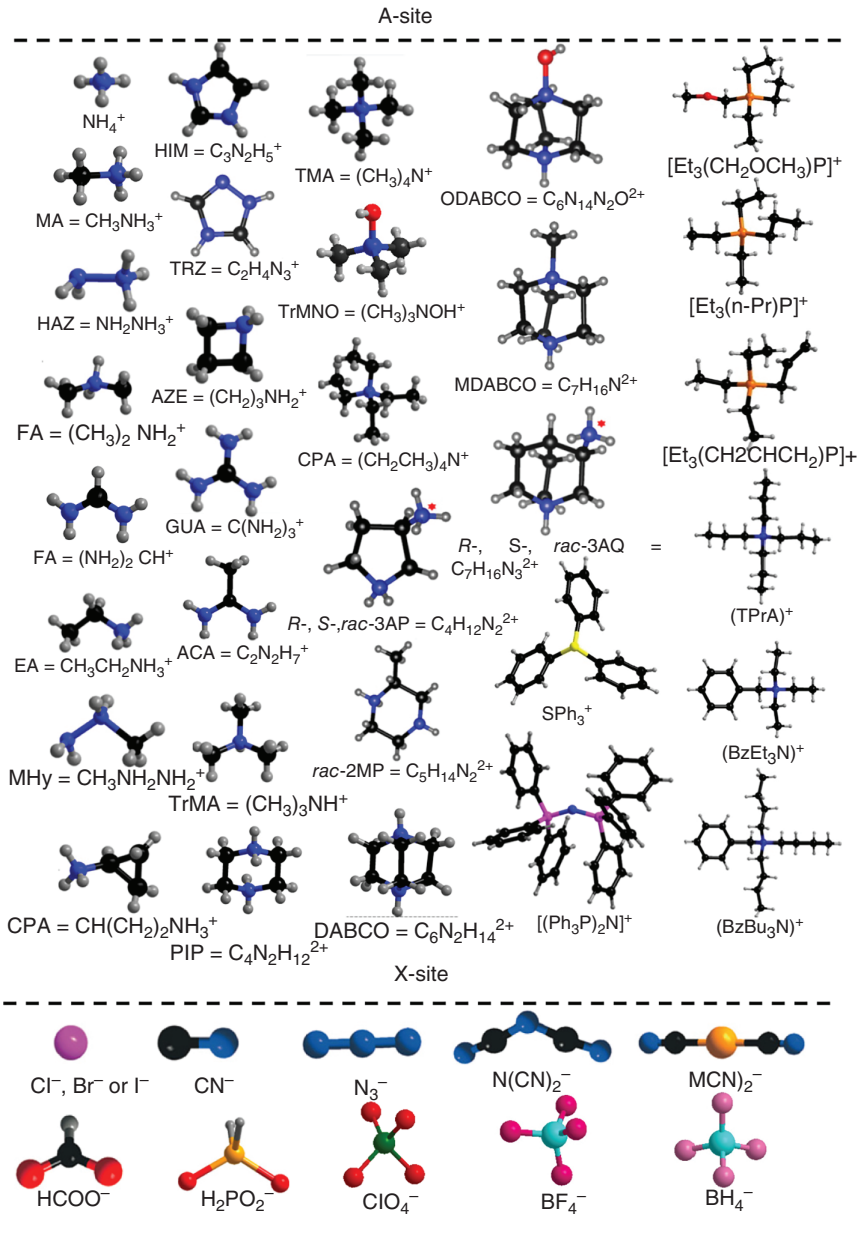

Figure 1.5 Structural diversity of the A-site and X-site ions of hybrid organic–inorganic perovskites. Colour schemes: N, blue; O, red; C, black; H, grey or light pink; Cl, purple or green; Br/I, purple; S, light yellow; P, yellow or purple; M = Ag or Au, yellow; B, turquiose; and F, pink.

the dca perovskites [18]. In terms of the X-site, they are all monovalent and can be monoatomic ion, biatomic group, and multi-atomic linkers (Figure 1.5). These X-sites include inorganic halide ion (Cl^-, Br^-, and I^-), cyanide ion (CN^-), azide ion (N_3^-), dicynametallate ion ($[Ag(CN)_2]^-$ and $[Au(CN)_2]^-$), borohydride

ion (BH_4^-), and organic formate ($HCOO^-$) and dicyanamide (dca^-) groups. Moreover, some ABX_3-type perchlorates and tetraborates can be topologically regarded as the perovskite-like compounds in which the perchlorate (ClO_4^-) and tetraborate (BF_4^-) serve as the B-site [19]. With respect to the B-site, most of them are divalent metal ions or mixed monovalent/trivalent metal ions, although few are monovalent metal ions because of the existence of organic diamine cations on the A-site. Interestingly, NH_4^+ can also serve as the B-site by octahedrally interacting with six halide ions to form metal-free perovskites with the templating organic diamine cations, $[A][(NH_4)X_3]$ (A^{2+} = organic diamine cation, $X^- = Cl^-$, Br^-, and I^-) [20].

The symmetries of HOIPs span all seven crystal systems, which are largely dependent on the size, shape, and nature of the A-site organic cations (Table 1.1). Specifically, organic amine cations with high symmetries (i.e. TMA) often lead to perovskite structures with high-symmetry space groups. In addition, the change of ordering state of the A-site organic amine cations can also result in symmetry alterations. For example, the switching from ordered to disordered states of MA in $MAPbI_3$ upon heating induces the symmetry change from orthorhombic to tetragonal, then to cubic. Like their inorganic counterparts, HOIPs can also exhibit diverse physical properties depending on their distinct compositions, which have been summarized in Table 1.1 [9]. Specifically, perovskite halides show remarkable optoelectronic properties, which have been intensively researched in the last 10 years. Perovskite formates demonstrate versatile magnetic properties, ferroelectricity and multiferroicity, as well as dielectricity.

Perovskite azides exhibit diverse magnetic properties and interesting ferroelasticity. Perovskite cyanides display various dielectricity and unique ferroelectric ordering. Dicyanamide perovskites show extraordinary barocaloric effects and associated solid-state cooling potential, as well as significant thermal expansion. All these striking properties of HOIPs are extensively discussed in the following chapters.

1.4.2 Ion Radius Matchability and Tolerance Factor

There are abundant variabilities of the A-, B-, and X-sites, and how to evaluate their matchability is a critical issue. According to the established criterion in perovskite oxides, the metric ratio of different ionic sizes, which can be tolerated by the perovskite lattice, is expressed by the Goldschmidt tolerance factor (TF, t) [21]. As the A-site and/or X-site in the HOIPs are not spherical ions but molecular groups, the t was adjusted to the following formula [22]:

$$t = (r_{Aeff} + r_{Xeff})/\sqrt{2}(r_B + 0.5\, h_{Xeff})$$

where r_B represents the radius of the B-site metal ion, and r_{Aeff}, r_{Xeff}, and h_{Xeff} stand for the effective radius of the A-site molecular group, the effective radius of the X-site molecular group, and the effective height of the X-site molecular group, respectively. As can be seen in Table 1.1, the calculations of TFs by summarizing all available A-site, B-site, and X-sites of known HOIPs demonstrate that most of their TF span is between ~0.8 and ~1.0. These results approximate those of

Table 1.1 Summary of the chemical variabilities, crystal symmetries, and physical properties of HOIPs [9].

HOIPs	A-site	B-site	X-site	Symmetry	TFs	Physical properties
Halides	MA, FA	Pb^{2+}, Sn^{2+}, Ge^{2+}	Cl^-, Br^-, I^-	Orthorhombic, trigonal, tetragonal, cubic	~0.912–1.142	Semiconductivity, photovoltaics, laser physics, light-emitting diodes, mechanical properties
	MA	K^+/Bi^{3+}, Tl^+/Bi^{3+} [a]			~0.906–0.923 [b]	
	PIP, DABCO	K^+, Cs^+, Rb^+	Cl^-	Monoclinic, orthorhombic, trigonal	~0.922–1.037	
Formates	K^+, Rb, Cs^+, NH_4^+, MA, FA, GUA, EA, DMA, AZE, HIM, HAZ, MHy	Mg^{2+}, Mn^{2+}, Fe^{2+}, Co^{2+}, Ni^{2+}, Cu^{2+}, Zn^{2+}, Cd^{2+}	$HCOO^-$	Monoclinic, orthorhombic, trigonal, tetragonal	~0.784–1.001 [c]	Magnetism, dielectricity, ferroelectricity, ferroelasticity, multiferroicity, mechanical properties
	MA, TMA, DMA, EA, HAZ, GUA, TMA	Na^+/Cr^{3+}, Na^+/Al^{3+}, Na^+/Fe^{3+}, K^+/Sc^{3+}, Cu^{2+}/Mn^{2+} [a]	$HCOO^-$	Monoclinic, triclinic, trigonal	~0.897–1.040 [b]	
Azides	MA, DMA, TEA, TrMA, TMA, CPA	Mn^{2+}, Cd^{2+}, Cu^{2+}, Ca^{2+}	N_3^-	Triclinic, monoclinic, cubic	~0.786–1.023	Magnetism, dielectricity, ferroelasticity
	TMA	Na^+/Cr^{3+}, Na^+/Fe^{3+}, K^+/Fe^{3+}, K^+/Cr^{3+} [a]			~0.934–1.008 [b]	
Dicyanamides	BPEA, BPTA, SPh_3, TPrA [d]	Mn^{2+}, Co^{2+}, Cd^{2+}, Fe^{2+}, Ni^{2+}	$[N(CN)_2]^-$	Monoclinic, orthorhombic, tetragonal	~1.142–1.166	Magnetism, dielectricity, non-linear optical, spin canted, barocaloric
Dicyanometallates	PPN	Cd^{2+}	$[Ag(CN)_2]^-$	Monoclinic, trigonal, cubic	~1.033–1.141 [d]	Magnetism
		Mn^{2+}, Co^{2+}, Ni^{2+}, Cd^{2+}	$[Au(CN)_2]^-$			

Cyanides	HIM, DMA, MA, TMA, TrMA, GUA, TEMA, ACA, TrMNO	K^+/Fe^{3+}, K^+/Co^{3+}, K^+/Cr^{3+}, Na^+/Co^{3+}, Na^+/Fe^{3+}, Rb^+/Fe^{3+}, Rb^+/Co^{3+}, Rb^+/Cr^{3+}, Cs^+/Cr^{3+}, Tl^+/Cr^{3+}, Tl^+/Fe^{3+} a)	CN^-	Triclinic, monoclinic, cubic, tetragonal	~0.840–1.031 b)	Dielectricity, ferroelectricity
Borohydrides	MA	Ca^{2+}	BH_4^- e	Cubic	~0.980	Hydrogen storage
Hypophosphites	FA, GUA, HIM, TRZ, DMA, DABCO	Mn^{2+}	$H_2PO_2^-$	Monoclinic, orthorhombic, triclinic, trigonal	~0.860–0.910	Magnetism
Perchlorates	PIP, H_2hpz , DABCO, ODABCO	K^+, Na^+, Rb^+	ClO_4^-	Orthorhombic, monoclinic, cubic	~0.914–1.015	Dielectricity, high-energetic
Tetrafluoroborates	PIP, DABCO	K^+, Na^+	BF_4^-	Trigonal, tetragonal, cubic	~0.913–1.050	Dielectricity
Metal-free perovskites	PIP, DABCO, ODABCO, *rac*-2MP, *R*-, *S*-, *rac*-3AP, *R*-, *S*-, *rac*-3AQ	NH_4^+	Cl^-, Br^-, I^- ClO_4^- BF_4^- ReO_4^-	Monoclinic, orthorhombic, trigonal, cubic	~0.870–1.000	High-energy, ferroelectricity, photoluminescence

HOIPs, hybrid organic–inorganic perovskites; TFs, tolerance factors.

a) Mixed B-sites in hybrid double perovskites.

b) The TFs of hybrid double perovskites, $A_2BB'X_6$, were calculated using the adapted formula $t = (r_{Aeff} + r_{Xeff})/\sqrt{2}(r_B/2 + r_{B'}/2 + 0.5\ h_{Xeff})$. $r_{Aeff} = r_{mass} + r_{ion}$, where r_{mass} is defined as the distance between the centre of the mass of the A-site organic molecule ion and the atom with the largest distance to the centre of mass (excluding hydrogen atoms), and r_{ion} is the corresponding ionic radius of the aforementioned atom. r_{Xeff} can be defined in a similar way as r_{Aeff}.

c) The unique tolerance factors of $KCo(HCOO)_3$, $CsCo(HCOO)_3$ and $[NH_4][Cd(HCOO)_3]$, which lie in the range ~0.620 to 0.700, are not presented in the table owing to the special *anti–syn* coordination mode of the formate linker.

d) Since the BPEA, BPTA, and SPh_3 cations are larger than the pseudo-cubic cavity, the relevant TFs were not able to be calculated.

e) The molecular structure of BH_4^- is not listed in the table because of the structural unavailability of $[MA][Ca(BH_4)_3]$.

conventional perovskite oxides and therefore indicate that such a semi-empirical rule can be extended to the hybrid systems. In other words, the lattice matchability and packing density primarily determine the formation of HOIPs. More importantly, this simple way can be facilely utilized to design new HOIPs, in which the rationally selected compositions with size compatibility can lead to desired functionalities. An expanded study of all possible A-site amine cations, B-site metal ions, and X-site anions across the periodic table reveals that several hundreds of HOIPs were yet to be discovered [23]. Following successive experimental discoveries of HOIPs with new physical properties have indeed demonstrated the validation of this powerful tool in synthesizing new functional HOIPs. For example, replacing toxic lead metal ion by mixed mono- and trivalent metal ions with benign nature keeps the size compatibility, and the obtained hybrid lead-free perovskite opens the possibility for addressing the environmental concern required for future industrial applications [24]. Nevertheless, special caution needs to be taken into account because such a simple metric is unable to fully reflect the lattice energetics and hence structure stability because of its empirical limitation.

1.4.3 Phase Transitions

As one of the most studied class of materials, perovskites exhibit almost all known physical properties. Importantly, many of these phenomena, such as ferroelectricity and ferromagnetism, arise from their structural phase transitions. The ideal perovskite has a very simple cubic O_h symmetry and is in a $Pm\bar{3}m$ space group. This parent high-symmetry aristotype architecture can evolve into a number of low-symmetry structures upon external stimuli, such as temperature and pressure. For conventional perovskites, their transitions are primarily driven by the displacement of the A- and/or B-site and the tilting of the BX_6 octahedral units. According to these two primary driving forces, Glazer and some others developed an appropriate group theoretical analysis to classify the symmetry breaking and phase transitions of inorganic perovskites [25, 26]. Through this approach, structure variations and the underlying mechanisms could be well defined, which could give a fairly powerful guide to experimentalists.

In terms of HOIPs, their phase transition mechanisms are complicated because of the existence of molecular ions on the A- and/or X-sites compared with their conventional counterparts. For hybrid perovskite halides, their X-sites are still monatomic anions; therefore, their octahedral tilting modes are reminiscent with the scenarios in oxide perovskites. However, the octahedra are not corner-shared any more when the X-site becomes a diatomic or multi-atomic linker, which significantly complicates the structural transition mechanisms. As expected, the long and large X-sites in HOIPs could lead to additional structural freedom for the octahedra and A-site organic amine cations to distort and shift. For example, neighbouring octahedra can distort along the same direction in some azide perovskites, and such an unusual octahedral tilting is impossible to occur in conventional perovskites [27]. Nevertheless, in most HOIPs, the octahedral tilting modes resemble those in oxides because the X-site molecular linkers are fairly rigid, which do not allow special rotation of adjacent octahedra.

Compared with the conventional perovskites, the displacements of the A- and B-sites in HOIPs are broadly similar, which usually involve the off-centre shift. However, the existence of organic molecular groups on the A-site complicates the situation as additional bonding interactions, such as hydrogen bonding and van de Waals forces, have to be taken into account. Such additional structural degrees of freedom often significantly affect the phase transition scenarios. Moreover, the A- and/or X-sites can also show dynamic motions, which involve significant entropic effect and hence being a strong phase transition driving force. The dynamic movement over different sites of the molecular group (including both the A- and X-sites) is defined as disorder, and many phase transitions of HOIPs are primarily driven by such an order–disorder process because of its aforementioned energetic effect. Notably, such an order–disorder process often involves alterations of hydrogen bonding and dispersion forces between the A-site and anionic perovskite framework, which could synergistically influence the symmetry breaking process [28]. Figure 1.6 shows the phase transition of [AZE][Cu(HCOO)$_3$] (AZE = azetidinium), as a typical example to showcase the synergistic mechanism. For the high-temperature *Pnma* phase, the AZE group exhibits a planar configuration with very large atomic displacement parameter of the side C2 atom (indicating a possible disorder of AZE at two sites over the N1–C1–C3 plane) and CuO_6 octahedra show a tilting system of $a^-b^+a^-$. Upon cooling, the structure evolves into the low-temperature $P2_1/c$ phase in which the AZE is fully ordered and the CuO_6 tilting becomes to $a^-b^+c^-$. During this symmetry breaking process, the order–disorder of AZE is the main driving force, and the associated hydrogen bonding changes also play a role. This kind of orthorhombic *Pnma* to monoclinic $P2_1/c$ transition is very rare as it requires the uncommon X-point modes in the Brillouin zone (while most transitions in conventional perovskites only involve the M- and R-point modes). Overall, the complex cooperation of various driving forces including displacement, octahedral tilting, and order–disorder leads to far more

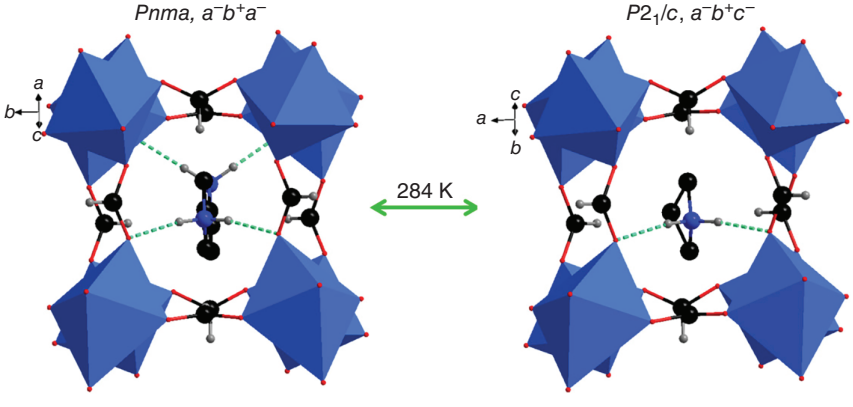

Figure 1.6 Phase transition mechanism in [AZE][Cu(HCOO)$_3$]. Colour schemes: N, blue; O, red; C, black; H, grey; and Cu, cyan. Source: Zhou et al. 2011 [31]. Reproduced with permission of John Wiley & Sons.

complicated phase transition mechanisms in HOIPs, in marked contrast to their inorganic counterparts [9].

More importantly, some special A-site organic amine cations are intrinsically polar so that bulk electric ordering could be obtained if they align in an ordered way through occurrence of phase transitions. This phenomenon is in marked difference to the displacive origin of electric ordering responsible for perovskite oxides. In addition, the alterations of hydrogen bonding and dispersion forces across phase transition play an important role in achieving such an ordered electric state. As expected, the obtained ferroelectric or anti-ferroelectric ordering strongly depends on the dipole moments carried by the A-site cations, along with other cooperative influences. Furthermore, the intimate cooperation of different bonding interactions from all sites in the structures of HOIPs during the symmetry breaking process could lead to ferroelasticity, multiferroicity, and many other novel properties, which are not possible in their conventional counterparts. These multiple bonding forces also play a pivotal role in modulating physical properties of HOIPs, which include magnetism, conductivity, and dielectricity [9, 29].

References

1 Rose, G. (1839). *De novis quibusdam fossilibus quae in montibus Uraliis inveniuntur*, 3–5. AG Schade.
2 Wenk, H. and Bulakh, A. (2004). *Minerals: Their Constitution and Origin*. Cambridge University Press.
3 Bhalla, A.S., Guo, R., and Roy, R. (2000). *Mater. Res. Innovations* 4: 3.
4 Hippel, A.V., Breckenridge, R.G., Chesley, F.G., and Tisza, L. (1946). *Ind. Eng. Chem.* 38: 1097.
5 Megaw, H.D. (1945). *Nature* 155: 484.
6 Glazer, A.M. and Mabud, S.A. (1974). *Acta Crystallogr.* B34: 1065.
7 Norby, P., Krogh Andersen, I.G., Krogh Andersen, E., and Andersen, N.H. (1995). *J. Solid State Chem.* 119: 191.
8 Frank, K. and Hans, S.H. (1990). *Acta Crystallogr.* B46: 698.
9 Li, W., Wang, Z., Deschler, F. et al. (2017). *Nat. Mater. Rev.* 2: 16099.
10 Weller, M.T., Weber, O.J., Henry, P.F. et al. (2015). *Chem. Commun.* 51: 4180.
11 Wang, Z., Zhang, B., Otsuka, T. et al. (2004). *Dalton Trans.* 15: 2209.
12 Javier, C., Sonia, P.Y., Garikoitz, B. et al. (2015). *Cryst. Growth Des.* 15: 2352.
13 Wang, Z.X., Zhang, Y., Tang, Y.Y. et al. (2019). *J. Am. Chem. Soc.* 141: 4372.
14 Wei, Z., Liao, W.Q., Tang, Y.Y. et al. (2018). *J. Am. Chem. Soc.* 140: 8110.
15 Batail, P. (1991). *Angew. Chem. Int. Ed.* 30: 1498.
16 Paton, L.A. and Harrison, W.T. (2010). *Angew. Chem. Int. Ed.* 49: 7684.
17 Wang, S.S., Huang, R.K., Chen, X.X. et al. (2019). *Cryst. Growth Des.* 19: 1111.
18 Tong, M.L., Ru, J., Wu, Y.M. et al. (2003). *New J. Chem.* 27: 779.
19 Sun, Y.L., Han, X.B., and Zhang, W. (2017). *Chem. Eur. J.* 23: 11126.
20 Ye, H.Y., Tang, Y.Y., Li, P.F. et al. (2018). *Science* 361: 151.
21 Golschmidt, V.M. (1926). *Naturwissenschaften* 21: 477.
22 Kieslich, G., Sun, S., and Cheetham, A.K. (2014). *Chem. Sci.* 5: 4712.

23 Shang, R., Chen, S., Wang, B. et al. (2016). *Angew. Chem. Int. Ed.* 55: 2097.
24 Wei, F., Deng, Z., Sun, S. et al. (2016). *Mater. Horiz.* 3: 328.
25 Glazer, A.M. (1975). *Acta Crystallogr.* A31: 756.
26 Howard, C.J. and Stokes, H.T. (1998). *Acta Crystallogr.* B54: 782.
27 Zhao, X.H., Huang, X.C., Zhang, S.L. et al. (2013). *J. Am. Chem. Soc.* 135: 16006.
28 Li, W., Zhang, Z., Bithell, E.G. et al. (2013). *Acta Mater.* 61: 4928.
29 Xu, W.J., Du, Z.Y., Zhang, W.X., and Chen, X.M. (2016). *CrystEngComm* 18: 7915.
30 Sasaki, S., Prewitt, C., and Bass, J.D. (1987). *Acta Crystallogr.* C43: 1668.
31 Zhou, B., Imai, Y., Kobayashi, A. et al. (2011). *Angew. Chem. Int. Ed.* 50: 11441.